Journal of Materials Chemistry C

ROYAL SOCIETY OF CHEMISTRY

PERSPECTIVE

View Article Online
View Journal | View Issue

Cite this: J. Mater. Chem. C, 2023, 11, 4993

Metal halide perovskites: promising materials toward next-generation circularly polarized luminescence

Bing Liang, [a] Li Zhang,[a] Yuanzhi Jiang, [a] Siqi Chen [a] and Mingjian Yuan *[ab]

Received 13th November 2022,
Accepted 2nd March 2023

DOI: 10.1039/d2tc04825f

rsc.li/materials-c

Metal halide perovskites (MHPs) have emerged as highly appealing materials for circularly polarized luminescence (CPL) related applications, owing to their spin-related photoelectric properties and flexible structural adjustment. However, the realization of high circular dichroic (CD) intensity and luminescence dissymmetry factors (g_{lum}) remains a challenge faced in the field of CPL material research, which greatly impedes the commercial application of perovskite-based CPL. In this perspective, we discuss the fabrication strategies of intercalating chiral organic ammonium into MHPs and chiral regulation of MHPs without chiral organic ammonium ligands, resulting in CPL emission. We then summarize the progress in circularly polarized light-emitting devices, mainly to realize high-performance CPL emission. These key challenges give rise to several promising research opportunities to facilitate the development of highly stable and high-performance CPL emitting devices, thus inspiring more possibilities for CPL display, cryptology, and anti-counterfeiting applications.

1. Introduction

Metal halide perovskites (MHPs) have become one of the most active areas of research attributed to their excellent photoelectric properties including high photoluminescence quantum yields (PLQYs), tunable emission, narrow emission spectrum, *etc.*[1–3] Simultaneously, these unique optical properties also provide potential material foundations for CPL applications. CPL refers to the phenomenon that represents the unequal emission of left- and right-handed polarized light (LCP and RCP) from an emitter. The most important parameters for evaluating the CPL system are luminescence efficiency (η_{CPL}) and the luminescence dissymmetry factor ($g_{lum} = 2[I_L - I_R]/[I_L + I_R]$, where I_L and I_R stand for the intensity of left-handed and right-handed circularly polarized light, respectively. The maximum value of g_{lum} is 2. CPL has extensive application prospects in the fields of three-dimensional (3D) displays, biosensing, encryption anti-counterfeiting, and photocatalytic

[a] Key Laboratory of Advanced Energy Materials Chemistry (Ministry of Education), Renewable Energy Conversion and Storage Center (RECAST), College of Chemistry, Nankai University, Tianjin, 300071, P. R. China. E-mail: yuanmj@nankai.edu.cn
[b] Haihe Laboratory of Sustainable Chemical Transformations, Tianjin, 300071, P. R. China

Bing Liang

Bing Liang completed her BS degree in Lanzhou Jiaotong University in 2020. She is currently an MS degree candidate in the College of Chemistry, at Nankai University, under the supervision of Professor Mingjian Yuan. Her research interest focuses on perovskite light-emitting diodes.

Mingjian Yuan

Mingjian Yuan pursued his post-doctoral research in the Department of Materials Science and Engineering at the University of Washington from 2009 to 2012, and then in the Department of Electrical Engineering and Computer Science, at the University of Toronto from 2012 to 2016. In 2016, he joined the College of Chemistry, Nankai University as a professor. Currently, his research focuses on organic–inorganic hybrid materials and optoelectronic devices.

asymmetry.[4–7] According to multiple studies, incorporating chiral organic ammonium cations into MHP frameworks can fabricate chiral MHP materials and generate CPL. Moreover, MHPs feature large Rashba splitting,[8] intrinsic strong spin–orbital coupling (SOC),[9] and long spin life,[10] which contribute to developing optoelectronic fields such as spintronic devices,[11] nonlinear optics,[12] and CPL lasers.[13]

In stereochemistry, chirality means that the structure of chemical compounds does not overlap with their mirror structure, and this symmetry breaking gives them circular polarization (CP) characteristics.[14–18] In 2003, Billing *et al.* reported chiral one-dimensional (1D) hybrid organic–inorganic perovskites (HOIPs) for the first time.[19] Subsequently, chiral two-dimensional (2D) perovskite single crystals were reported in 2006.[20] Since then, 3D metal-free perovskites,[21] low-dimensional perovskites,[22] chiral perovskite nanocrystals (NCs),[23] and cogels[24,25] have been reported successively. However, the underlying origination of chirality has not been discussed in depth, which greatly impedes the research of chiral perovskites. Generally, CPL properties can be achieved in perovskites by directly using chiral organic ammonium cations to break the intrinsic symmetry of the MHPs' structure.[26–28] Nevertheless, this straightforward method may lead to inferior quality CPL with a low circular dichroic (CD) intensity and luminescence dissymmetry factors (g_{lum}), if there is a lack of effective theoretical guidance and design. The issue herein urgently requires remedy.[4,24]

We review the recent research progress and summarize two promising strategies for MHPs in the field of CPL applications, including intercalating chiral organic ammonium into MHPs and chiral regulation of MHPs without chiral organic ammonium ligands. The former essentially introduces the spin electrons of chiral organic ammonium into MHPs to break the symmetry of MHP structures. Besides, the wavelength range of the CD signal can be regulated precisely by adjusting the ratio of mixed halogens to achieve full-color CPL.[29,30] Moreover, manipulating the crystallization kinetics of the perovskite films could also promote the enhancement of the CD signal intensity.[31] As for the chiral regulation of MHPs without chiral organic ammonium ligands, the researchers investigated the spin-dependent excitation dynamics to figure out the mechanism inside. Magnetic material-doped (Mn^{2+}, Cu^{2+}, Fe^{2+}, *etc.*[32–34]) MHPs are capable of achieving unbalanced exciton spin distribution by delaying relaxation among excitons. Strong CP comes from interactions between magnetic material-doped MHPs and isolated dopant cations.[35] In addition, chirality-introduced energy transfer strategies are used to amplify the CD signals. Novel strategies comprise upconversion-induced fluorescence,[36,37] control spin-relaxation-dynamics for CP,[38,39] and a dry transfer stacking technique.[40]

Obtaining a large degree of CP and efficient chiral circularly polarized emission is also difficult. Several researchers have concentrated on investigating the effect of circularly polarized emissions *via* various compact devices. For instance, obtaining narrow mode positions of Chiral Fano Resonance by perovskite precursors spin coated on symmetry-broken templates, implementing more than a large degree of CP (>0.5) at room temperature.[41]

It not only increases the helicity of the material but also improves the photoluminescence (PL) intensity of LCP and RCP. Notably, considerations such as how to achieve a high circularly polarized electroluminescence (CPEL) efficiency of MHPs are presented. As is well known, the realization of spin-induced electroluminescence (EL) often requires an applied magnetic field. Based on the chiral-induced spin selectivity (CISS),[42] a chiral carrier collector is built to produce spin-polarized carriers and avoid spin dephasing at the device interface.[43] Finally, spin-induced CPL was obtained at room temperature without magnetic fields or ferromagnetic contacts.[44]

The CD signal intensity and the g_{lum} values of the perovskite-based CPL are much lower than their theoretical maxima, which strongly hinders the practicality of CPL. In addition, investigation of the underlying mechanism of chirality appears to be particularly important. Following this trend, we discuss the two general strategies that can imprint chirality onto the electronic states of perovskites,[7] resulting in CPL emission at the beginning.[45] We then summarized the progress in circularly polarized light-emitting devices, mainly to realize high-performance CPL emission. Finally, we discuss the key challenges in the field and propose several promising research opportunities to facilitate the development of highly stable and high-performance CPL emitting devices. This perspective article thus paves the way for future perovskite-CPL emitter manufacture.

2. Intercalating chiral organic ammonium into MHPs

For chiral material films, the absorption sensitivity to circularly polarized light was quantified by the absorption dissymmetry factor (g_{abs}) or *g*-factor. g_{abs}[46] often serves as the evaluation of CPL absorption materials, facilitating the development of CPL materials with high dissymmetry. D is defined as each transition between the emissive state (j) and ground state (i) (eqn (2)[47]). $\boldsymbol{\mu}$ refers to an electric dipole,[48] $\boldsymbol{m}$ refers to a magnetic dipole[49] and $\boldsymbol{c}$ is the speed of light and the sign relates to left-/right-handed CPL, $\boldsymbol{\theta}$ refers to the angle between $\boldsymbol{\mu}$ and $\boldsymbol{m}$. R is the scalar product of the $\boldsymbol{\mu}$ and $\boldsymbol{m}$ (eqn (1)[50]). Typically, $\boldsymbol{\mu}$ is much larger than $\boldsymbol{m}$. Because $|g_{abs}|$ and $|g_{PL}|$ are proportional to each other,[51] this results in nanomaterials possessing small $|g_{PL}|$ values.[52] For many small organic molecules, a high ψ_F (fluorescence quantum yield)[53] corresponds to a high D. However, $\boldsymbol{\mu}$ is often greater than $\boldsymbol{m}$.[54,55] This usually results in a low g_{PL} value (eqn (3)).[30,51]

$$R = |\boldsymbol{\mu}||\boldsymbol{m}|\cos\theta \tag{1}$$

$$D = \left|\left\langle \psi_j \middle| \boldsymbol{\mu} \pm \left(\frac{i}{\boldsymbol{c}}\right)\boldsymbol{m} \middle| \psi_i \right\rangle\right|^2 \tag{2}$$

$$g_{abs} = 4 \times \frac{R}{D} = \frac{4}{c}\frac{|\boldsymbol{m}||\boldsymbol{\mu}|}{\boldsymbol{\mu}^2 + \left(\frac{\boldsymbol{m}}{\boldsymbol{c}}\right)^2}\cos\theta \approx \frac{4|\boldsymbol{m}|}{c|\boldsymbol{\mu}|}\cos\theta \tag{3}$$

In the process of studying chiral perovskites, efforts have been devoted to constructing MHPs materials, which possess

CPL with high g_{lum} values, aiming at CPL applications.[56] Chirality can be introduced into MHPs *via* the following strategies: intercalating chiral organic cations into the perovskite lattice[30,31,57] and modifying the surface of perovskite crystals with chiral ligands,[36,58–60] which could all imprint chirality onto electronic states of perovskites, which all result in CPL emission with high PLQY.[61] The introduction mechanism consists of the following aspects: electron coupling between the chiral organic molecules and the inorganic structure,[62] chiral distortions of the inorganic surface,[63] and chiral patterning of the surface ligands.[64]

2.1. Introducing chiral organic ammonium to low-dimensional MHPs

Ordinarily, incorporating chiral organic ammonium into MHPs can induce the generation of chirality.[65] In this process, the centrosymmetric structure of MHPs was broken, forming dissymmetric crystal structures and chiral space groups, which give MHPs different physical and optical properties.[25] In addition, mixed halogen tuning can regulate the wavelength range of chiral HOIPs and good crystallization quality can further enhance the CD intensity of chiral HOIPs.

It is considered that α-phenylethylamine (α-PEA) organic ammonium molecules possess conjugated π-bonds. The Coulomb gravitational interactions exist between the chiral organic ammonium (*R*- and *S*-)-α-PEA molecules and the inorganic $(PbI_6)^{4-}$ octahedral structures, which are administered to enhance the sensitive CD absorption intensity of HOIPs. In 2019, Tang *et al.* fabricated (*R*- and *S*-PEA)PbI_3 single crystals utilizing an inverse-temperature crystallization method.[57] Then the chirality of (*R*- and *S*-α-PEA)PbI_3 perovskites was confirmed from the chiral $P2_12_12_1$ space group with the orthogonal structure. As CD absorption spectra are shown, the CD absorption peaks positions of (*R*- and *S*-α-PEA)PbI_3 perovskites (328 nm and 392 nm), which are different from the CD absorption peak position of α-PEA (259 nm). Finally, the fabrication of (*R*- and *S*-α-PEA)PbI_3 single crystals obtained a high responsivity of 797 mA W^{-1} and a high detectivity of 7.1×10^{11} Jones, which were expected to be applied in chiral perovskites photodetectors. Ma *et al.* fabricated needle-like, millimeter-sized 2D (*R*-/*S*-MBA)$_2PbI_4$ ($n = 1$) chiral perovskite crystals, in which the molar ratio of chiral organic ammonium phenylethylamine cations (*R*-/*S*-MBA^+) accounted for 67% of the total fraction. A higher percentage of organic matter makes 2D (*R*-/*S*-MBA)$_2PbI_4$ ($n = 1$) perovskites have a stronger CD signal intensity than chiral low-dimensional ($n \geq 2$) perovskites.[67,68] It can be attributed to the fact that the mixed phase in the latter not only induces spin electron flipping but also the grain boundaries in thin film samples inevitably enhance spin-flip. Subsequently, the authors explored the trend of the CP for 2D (*R*-/*S*-MBA)$_2PbI_4$ perovskites with temperature changes. At 77 K, the average CP of chiral 2D (*R*-MBA)$_2PbI_4$ and (*S*-MBA)$_2PbI_4$ perovskites are 9.6 and 10.1%, respectively. Whereafter, with the temperature increasing, the chirality transfer effect of *R*- and *S*-MBA^+ cations on perovskites gradually diminished. Until it approached room temperature, the chirality signal nearly disappeared. Correspondingly, it is inferred that the varying CP degree of (*R*-/*S*-MBA)$_2PbI_4$ perovskites includes two aspects: the concerned introduction of *R*- and *S*-MBA^+ cations and the temperature-induced spin flip-induced lattice distortion. However, the exact mechanism needs to be further explored. Finally, to effectively separate the photogenerated carriers, the authors prepared a heterojunction of chiral 2D (*R*-/*S*-MBA)$_2PbI_4$ perovskite microplate/MoS_2, which is applied in the CPL detector device. It successfully demonstrated that the fabricated chiral single-crystal device can effectively and selectively detect CPL at room temperature. This work lays a foundation for the development and exploration of chiral 2D perovskite-relevant spin-related electronic devices.[68]

Compared to α-PEA organic ammonium molecules, 1-(1-naphthyl)ethylamine (NEA) has a large molecular size. In 2D (*R*-/*S*-NEA)PbI_4 perovskites, large π-conjugated naphthalene skeletons could strongly interact with neighbor molecules, thus influencing the distortion of the $(PbI_6)^{4-}$ octahedral structure, which will enhance the helicity of the $(PbI_6)^{4-}$ octahedral structure. In 2021, T. Miyasaka *et al.* fabricated 1D (*R*- and *S*-NEA)PbI_3 and 2D (*R*- and *S*-NEA)$_2PbI_4$ perovskites by controlling the molar ratios of PbI_2 to chiral organic ammonium *R*-/*S*-NEA^+ cations with 0.5–2.0 and 1, respectively.[31,69] For 1D (*R*- and *S*-NEA)PbI_3 perovskite, the introduction of *R*- and *S*-NEA^+ cations greatly affected the helicity of the face-shared connected octahedral $(PbI_6)^{4-}$ structure, resulting in (*R*- and *S*-NEA)PbI_3 forming a chiral space group of $P2_12_12_1$. In the process of fabricating 1D (*R*/*S*-NEA)PbI_3 perovskites by mixing the molar ratio of (*R*/*S*-NEA)I and PbI_2, considering that the 2D structure generation rate may be faster than that of the 1D structure, the crystallization rate of the 1D perovskite film would be controlled correctly by adding a small amount of 0.05–0.1 M methylammonium iodide (MAI). Note that 1D perovskites possessing a smooth surface were obtained attributed to adding methylammonium (MA) to the perovskite precursor fluid and the formation of $MAPbI_3$ occurs with the 1D perovskites. Therefore, the corresponding absorption peak at 500 nm of 1D (*R*-/*S*-NEA)PbI_3 comes from $MAPbI_3$ (Fig. 1b). The X-ray diffraction (XRD) testing demonstrates that 1D (*R*-/*S*-NEA)PbI_3 perovskites with a small amount of MAI have a better crystallinity than the 1D perovskites without MAI. Note that the intensity of the CD signal of the 1D perovskites with MAI is 10 times that of the 1D perovskites without MAI. The CD absorption spectra show that the 1D perovskites have a stronger CD absorption peak intensity which is more than 3000 mdeg at 395 nm compared to the CD absorption peak intensity of 2D perovskites at 488 nm (Fig. 1b). In other words, the molar ratio of PbI_2 to NEA^+ (0.75 : 1) resulted in 1D (*R*-/*S*-NEA)PbI_3 perovskites possessing the CD dissymmetry factor (g_{CD}) of 0.04.

In 2022, Qin *et al.* reported that (*R*- and *S*-$[BPEA]_2PbI_4$ (BPEA = 1-(4-bromophenyl)ethylamine)) perovskites can exhibit significant CPL emission at ~513 nm (Fig. 1f).[66] At room temperature, the maxima polarization degree is up to 11.0%. Both *R*-$[BPEA]_2PbI_4$ and *S*-$[BPEA]_2PbI_4$ perovskite enantiomers crystallize in the chiral *C*2 space group (Fig. 1d). The chirality of *R*-$[BPEA]_2PbI_4$ and *S*-$[BPEA]_2PbI_4$ was defined by CD absorption spectroscopy and the measured results (Fig. 1e) show that *R*-$[BPEA]_2PbI_4$ and *S*-$[BPEA]_2PbI_4$ have the opposite CD degree at the same absorption

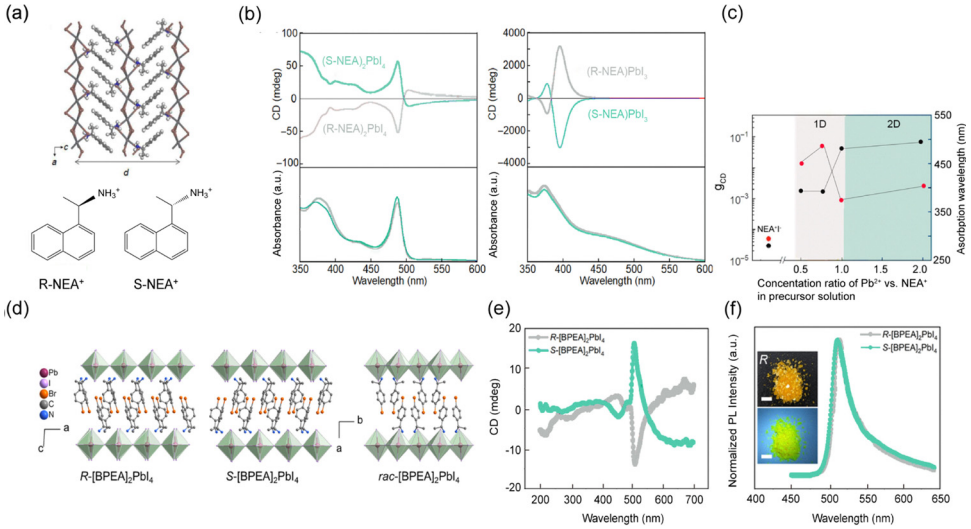

Fig. 1 (a) The structural model of 1D (*R*-NEA)PbI_3 in the *ac* plane. Molecular structure of *R*-NEA^+ and *S*-NEA^+ cations. (b) CD and absorption spectra of 2D (*S*- and *R*-$NEA)_2PbI_4$ and 1D (*S*- and *R*-NEA)PbI_3 perovskites. (c) The value of g_{CD} factor (red dots) and absorption wavelength (black dots) for the concentration ratio of Pb^{2+} to NEA^+ in the precursor solution. Reproduced with permission from ref. 31. Copyright 2020, American Association for the Advancement of Science. (d) Schematic of the crystal structures of *R*-, *S*-$[BPEA]_2PbI_4$, and *rac*-$[BPEA]_2PbI_4$ perovskites, respectively. (e) CD signals of chiral (*R*, *S*)-$[BPEA]_2PbI_4$ perovskites. (f) Steady-state PL spectra of (*R*, *S*)-$[BPEA]_2PbI_4$ perovskite thin films. Inset pictures represent optical images of *R*-$[BPEA]_2PbI_4$ crystals under white light (upper) and 365 nm UV illumination (bottom). Scale bars, 5 mm. Reproduced with permission from ref. 66. Copyright 2022, American Chemical Society.

wavelength. Furthermore, due to the polar crystal structures of *R*-$[BPEA]_2PbI_4$ and *S*-$[BPEA]_2PbI_4$, they are expected to exhibit a piezoelectric response. This proved to be a functional component in the mechanical energy harvesting device.[70]

2.1.1. Halogen tuning of chiral low-dimensional MHPs. A mixed halogens (Cl^-, Br^-, I^-) strategy enables induced changes in the perovskites crystal structures by adjusting the ratio of different mixed halogen anions. Furthermore, it can tune CD emission wavelength by changing the band gap of chiral HOIPs. As is shown in Fig. 2a, when the mixed halogen ions are tuned to the iodide-determinant phase and bromide-determinant phase, the CD signal can produce "turn on" and "turn off" functions.[29] In conclusion, some investigations show that the mixed halogens tuning of chiral HIOPs affects the chiral optical properties of chiral HIOPs in two ways: (1) regulating the wavelength of CD by regulating the exciton band structure,[71,72] and (2) opening and closing the CD signal by inducing changes in the crystal structure.[73] These properties facilitate the construction of chiral optical materials with color-tunable CD emission properties, which are expected to be applied to spin-polarized optical devices.[30]

Note that Moon *et al.* studied the optical properties changes of $(S\text{-}/R\text{-MBA})_2PbI_{4(1-x)}Br_{4x}$ (x = 0, 0.1, 0.2, 0.3, 0.4, and 0.5) perovskites based on a mixed halogens strategy.[29] Perovskites' excitonic absorption band gap was altered by adjusting the mixed ratio of Br^- and I^- anions. As is shown in Fig. 2b, the CD absorption peak position shifts from 495 nm to 474 nm when x was increased from 0 to 0.3. However, the crystal structures of chiral HOIPs shift and the CD signal is turned off when the iodide-determinant phases transfer to the bromide-determinant phase. To broaden the adjustability of the CPL of chiral HOIPs less than the wavelength of 474 nm, the authors utilized larger size NEA^+ cations instead of MBA^+ cations as insert layers to fabricate $(S\text{-}/R\text{-NEA})_2PbI_{4(1-y)}Br_{4y}$ (y = 0, 0.3, 0.5, 0.7, and 1.0) perovskites. Thus, increasing the spacer sizes between MBA^+ cations in layered perovskites, thereby increasing the band gap of chiral HOIPs. When y = 1, the CD signal peak position of $(S\text{-}/R\text{-NEA})_2PbI_{4(1-y)}Br_{4y}$ can be blue-shifted to 375 nm.[29]

In 2021, Qiu *et al.* constructed $[(R/S)\text{-(XMBA)}]_2PbI_4$ perovskites by introducing various chiral organic ammonium halide cations ($(R/S)\text{-}XMBA^+$, X = F^-, Cl^-, Br^-, I^-) to $(PbI_6)^{4-}$ octahedral structures.[30] They investigated that different halogen-substituted opposite positions of H-atoms in benzene rings of MBA molecules have effects on CPL. Correspondingly, three samples of $(ClMBA)_2PbI_4$, $(BrMBA)_2PbI_4$, and $(IMBA)_2PbI_4$ were fabricated and the maximum CD signal intensities are 90 mdeg, 60 mdeg, and 30 mdeg, respectively. The different CD signal intensities of chiral $(XMBA)_2PbI_4$ (X = F^-, Cl^-, Br^-, I^-) are determined as follows: $ClMBA^+$, $BrMBA^+$, and $IMBA^+$ cations have different magnetic transition dipole moments attributed to different halogen atom substitutions. Thanks to the *g*-factor of $(XMBA)_2PbI_4$ (X = F^-, Cl^-, Br^-, I^-) being proportional to the magnetic transition dipole moment. Among the four samples explored, the $(FMBA)_2PbI_4$ sample has a minimal CD signal intensity of 10 mdeg. It is well explained that the $(ClMBA)_2PbI_4$ sample has a maximum magnetic transition dipole moment, and the *g*-factor reached 3.1×10^{-3}. In addition, the counter-point replacement from Cl^- to I^- anions gradually increases the interlayer *d*-spacing distance of $(XMBA)_2PbI_4$ perovskites, thereby reducing the rotational strength of the $(XMBA)_2PbI_4$ structure. Hence, the selection to introduce Cl^- anions in the MBA molecular counterpoint can strengthen interactions between layers and layers, resulting in a significant increase in rotational strength. In a word, chiral $(ClMBA)_2PbI_4$

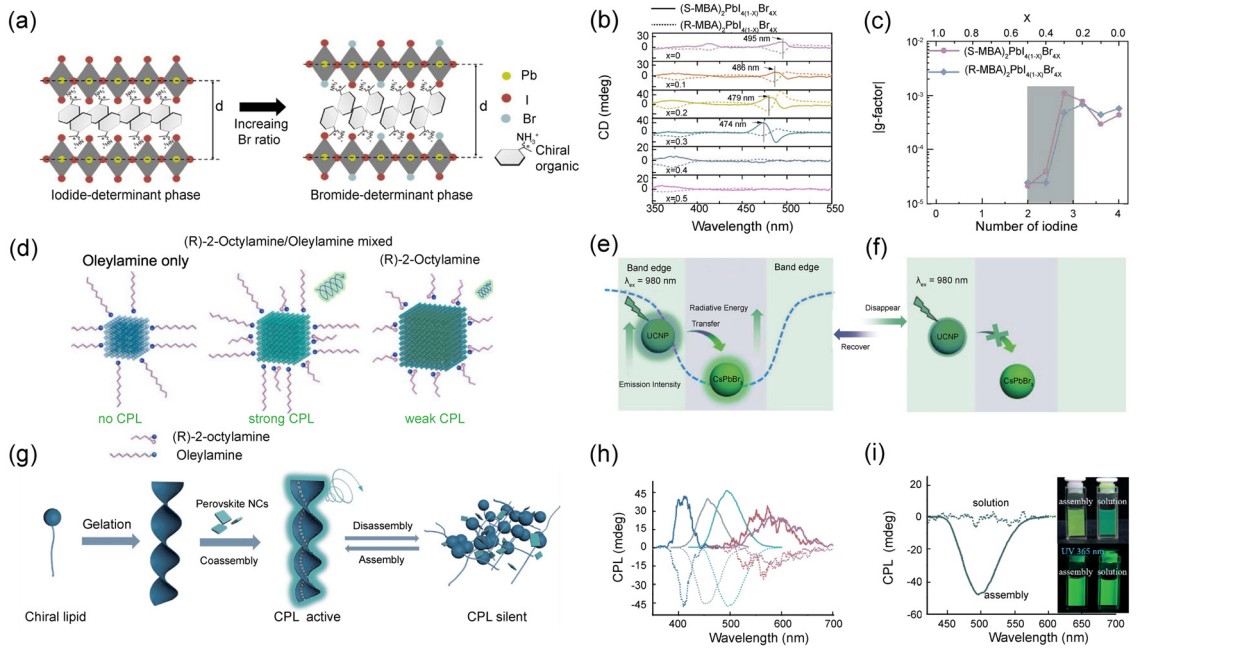

Fig. 2 (a) A schematic illustration of the phase transition with an increasing bromide ratio. (b) The CD spectra of (*S*-/*R*-MBA)$_2$PbI$_{4(1-x)}$Br$_{4x}$ (x = 0, 0.1, 0.2, 0.3, 0.4, 0.5). (c) Absolute values of the g-factors concerning the amount of iodine in the (*S*-/*R*-MBA)$_2$PbI$_{4(1-x)}$Br$_{4x}$ ($0.0 \leq x \leq 1.0$) perovskites. Reproduced with permission from ref. 29. Copyright 2020, American Chemical Society. (d) The ligands of oleylamine only, (*R*)-2-octylamine/oleylamine mixed, and (*R*)-2-octylamine only control the synthesis of FAPbBr$_3$ NCs. Reproduced with permission from ref. 58. Copyright 2020, American Chemical Society. (e and f) To achieve a high g_{lum} value of UC-CPL as well as enhanced emission intensity, CsPbBr$_3$ PKNCs and UCNPs were used as the energy acceptors and donors, respectively. Due to the weaker emission of UCNPs after applying an electric field, the UC-CPL emission could be switched off. Reproduced with permission from ref. 36. Copyright 2020, Wiley-VCH. (g) The illustration of co-assembly chiral gels and perovskite NCs. Then the doped NCs might follow the chirality of the gel structure to produce chiral packing that would lead to the induced chirality of NCs. In particular, CPL could be switched *via* heating or cooling the cogel. (h) The CPL spectra of the corresponding coassembly sample. λ_{ex} = 310 nm. (i) The CPL spectra of assembly and disassembly green-CsPbX$_3$ NCs doped DGAm, respectively. Solvent refers to chlorobenzene. [DGAm] = 4.6 mM, [CsPbX$_3$ NCs] = 1.1 mg mL^{-1}. The inset images represent the cogel and solution samples under light (top) and UV light (bottom, 365 nm), respectively. Reproduced with permission from ref. 23. Copyright 2018, Wiley-VCH.

perovskite has the highest magnetic transition dipoles and the highest rotational strength, further effectively affecting the intensity of the CD signal of HOIPs. Meanwhile, this work demonstrates that the intensity of CD and CPL signals can be controlled effectively by systematic screening for the organic cations.

2.2. Incorporating chiral organic ligands into MHP nanocrystals (NCs)

Chiral molecules as MHP NCs' surface ligands could introduce the optical activity in MHP NCs in the following two ways: near-surface lattice enantiomeric distortions or electronic coupling between the chiral ligands and NCs.[45,74,75] Generally, the conventional strategy is to use chiral organic ammonium ligands to construct CPL-active MHP NCs during synthesis, followed by ligands exchange. Notably, this strategy is prone to induce polarization characteristics in the ground state and it is not easy to induce polarization characteristics in the excited state of NCs.[60] Generally speaking, the fabrication of chiral quantum dots (QDs) is through the use of chiral organic ammonium ligands to seal the end to generate CD signals, but a slight change in the sealing reagent will lead to a change in the CPL signal.[58,76] Consequently, it is difficult to fabricate chiral MHP NCs with a stable structure by modification of the sealing reagent.[61] Therefore, careful design of the chiral matrix is required to ensure that the front-line molecular orbitals of chiral organic ligands match the band edge energy levels of MHP NCs.[77] For instance (Fig. 2d), in the process of FAPbBr$_3$ NCs synthesis, Kim *et al.* replaced a fraction of a typical ligand (oleamine) with a short chiral organic ligand (*R*-2-octylamine), which results in small monodisperse NCs producing high CPL with $g_{lum} = 6.8 \times 10^{-2}$.[58] Afterwards, the authors found that the chiral ligand was removed during the post-synthetic purification process, which in turn led to the decrease in CPL. Thus the authors employed (*R*-/*S*-)-methyl benzyl ammonium bromide (*R*/*S*-MBA: Br) to recover left and right CPL with an average $g_{lum} = \pm 1.18 \times 10^{-2}$ from purified NCs. Hence, we could conclude that modifying the surface of perovskite crystals with chiral ligands is an important way to imprint charity onto the electronic states of perovskites. Besides, Kim *et al.* also demonstrated that the chiral matrix of MHP NCs was shown to be one of the important factors affecting the g-factor, crystallinity, and helical symmetry of the material. To date, several new strategies have concentrated on co-assembly of MHP NCs with chiral matrices such as chiral gels,[23,60] metal–organic frames,[78] columnar liquid crystals,[36] *etc.* Excitingly, in 2018, Shi *et al.* discovered a phenomenon in which chiral

N,*N*′-bis(octadecyl)-L-glutamic diamide (LGAm) molecules or its enantiomer DGAm molecules and the achiral perovskite $CsPbX_3$ (X = Cl, Br, I, Cl/Br, and Br/I) NCs can assemble into amphoteric molecules together in non-polar solutions[23,79] (Fig. 2g). During the assembly process, such chiral gel molecules can aggregate on the achiral perovskite $CsPbX_3$ NCs surface and modify the surface of NCs. Then the chiral signal was transferred from chiral gel molecules to the achiral perovskite NCs, constructing stable chiral perovskite NCs. Notably, MHP NCs can be endowed with the corresponding chiral characteristics by modulating the chirality of gel molecules. In particular, when the absorption and emission peak locations of achiral $CsPbBr_3$ NCs overlap with those of chiral gels,[60] stronger CD absorption intensity and CPL emission signal can be generated. As a result, the achieved g_{lum} is as high as 10^{-3}. This work provides a new perspective and a new strategy for the design of novel functionalized chiroptical nanomaterials.[79]

3. Chiral regulation of MHPs without chiral organic ammonium ligands

Besides the introduction of chiral organic ammonium ligands to MHPs to produce CPL, we herein are concerned with the chiral regulation of MHPs without chiral organic ammonium ligands *via* regulating spin electrons,[39,80] the chiral energy transfer strategy,[39,81] and spin-relaxation dynamics for CP.[82]

3.1. Regulating spin electrons

The triplet state is composed of linearly and two orthogonally polarized components.[83] Particularly, the triplet-state excitons are usually optically active in MHPs.[84,85] Furthermore, the bright excitons in perovskite materials could provide perovskites with spin sublevels, thereby generating radiative transitions carrying the angular momentum. That is to say, when bright excitons are split into excitons at different energies, the photoexcitation population at the sublevel will be governed by the Boltzmann distribution and lead to polarized PL.[86] As a result, the photo-excited particles on the sub-energy level tend to be balanced resulting in the limit of perovskites' tolerance factors. Based on the above explanation, it is necessary for the application of external factors to disrupt the equilibrium of photoexcited particles on the sub-energy level. Recently, scientists have proposed that the equilibrium population of photo-excited particles can be broken by the energy splitting of energy levels under external fields.[87] Under an external magnetic field of MHPs are capable of causing energy splitting at the spin sub-energy level of the triplet state exciton, which is similar to structure-induced zero-field splitting,[83] also known as the Zeeman effect of excitons.[88,89] Exceptionally, if MHP lacks Zeeman effects under external magnetic fields or lacks inversion symmetry/Rashba effect, energy splitting will probably be larger than the zero-field splitting, leading to the destruction of the simplicity of the bright triplet state.[90]

Ultimately, photoexcited particles of MHPs could obtain an unbalanced sub-energy level population by the strategy of magnetic material doping, which is achieved by employing non-lead elements (Mn,[91] Ni,[92] Sn,[93] Cu,[94] *etc.*) to substitute Pb elements.[90,95,96] Essentially, there is a direct exchange of electrons (sp-d exchange) between the local dopant and the conduction band or valence band of the host semiconductor, and spin sub-bands are proportional to the magnetization of the material and can be up to dozens of meV, which leads to the inhomogeneous thermal occupation of the energy transfer spin state leading to CPL emission.

Transition metal doping as a strategy was shown to alter the photoelectric properties of MHPs. For example, manganese-doped $MAPbI_3$ [MA(Mn:Pb)I_3] single crystals possess the signatures of photo-switchable ferromagnetism (T_c = 25 K),[98] suggesting a coupling between the dopants' d electrons spin and optically excited $MAPbI_3$ perovskites' charge carriers. In addition, MA(Mn:Pb)I_3 single crystals have a 15% saturation polarization at 4 K and 6 T, indicating MA(Mn:Pb)I_3 possesses a highly unbalanced spin population. The strategy of manganese doping has been proven to enable the control of the exciton spin state of Ruddlesden-Popper (RP) perovskites effectively. In 2021, Neumann *et al.* successfully induced the paramagnetic properties of the diamagnetic $(PEA)_2PbI_4$ (PEPI) perovskite by adding a small amount of manganese salt to the precursor solution. Then, they investigated that Mn^{2+} doped PEPI could interact with isolated Mn^{2+} cations modulating the spin physics and the fine structure of excitons in PEPI (Fig. 3a).[35] Afterward, it could essentially delay the relaxation between exciton energy levels, since there is a weak coupling between magnetism doping MHPs and the optical properties of MHPs. In the paramagnetic 2D manganese-doped $(PEA)_2PbI_4$ (Mn:PEPI) perovskites, there is a strongly circularly polarized magnetically brightened excitonic luminescence produced by interaction with isolated Mn^{2+} ions. Further magnetic testing showed that a dark exciton population is brightened by mixing with the bright excitons in the presence of a magnetic field. The saturation polarization of Mn:PEPI perovskites is 13% at 4 K and 6 T. The measured magnetization does not show hysteresis behavior when scanning the magnetic field (Fig. 3c), which corresponds to the spin alignment of the high-spin Mn d^5 configuration in the magnetic field.

The authors studied spin-related exciton kinetics to verify the phenomenon that Mn:PEPI produces strong circularly polarized magnetic brightening exciton luminescence.[99] It should be noted that the magnetic intensity of the material is proportional to the CP degree. For the first time, Mn^{2+} cation doping can induce excitons to spin overturn, and the spin excitations structure of the Mn^{2+} doped PEPI sample is finely altered accordingly. The production of CPL relies on ultrafast spin processes also demonstrated simultaneously. Secondly, the transfer extent of Zeeman energy between different spin bands is proportional to the magnetization intensity of the material.[100] To prove this conjecture, the authors designed an experiment as follows: at a strong magnetic field, the doped Mn^{2+} sample possesses a small displacement compared to the undoped sample. The above phenomenon proves the presence of the dark exciton spin sub-state. The formation of dark excitons may come from light-excited free carriers or bright excitons. Hence, an sp-d exchange could be negligible in Mn^{2+}

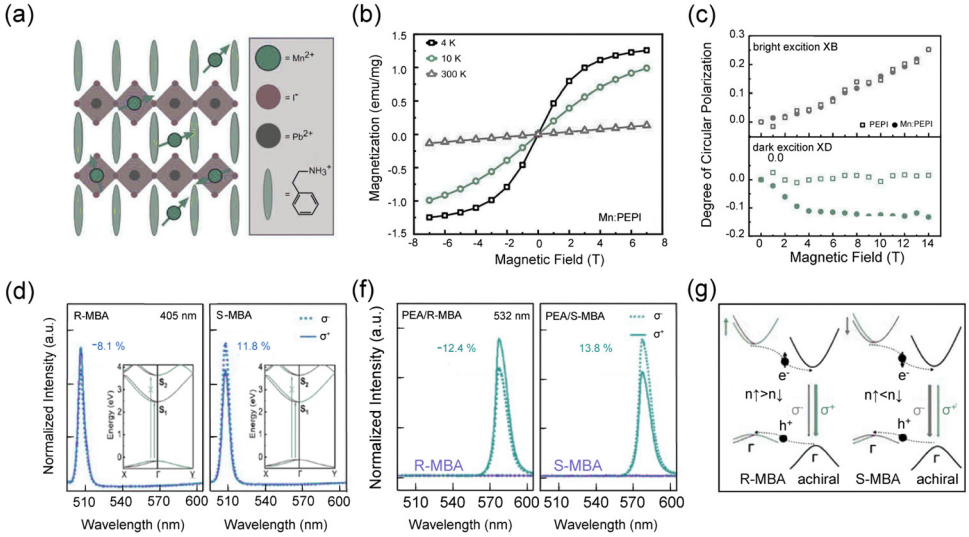

Fig. 3 (a) Sketch of the Ruddlesden–Popper quantum well structure with two possible Mn sites consisting of substitutional for the divalent anion and interstitial in the organic barrier. (b) The magnetization of Mn:$(PEA)_2PbI_4$ (Mn:PEPI) *versus* field sweep at different temperatures. (c) Comparison of undoped PEPI and Mn:PEPI for the bright (top) and dark (bottom) exciton emission. Reproduced with permission from ref. 35. Copyright 2021, Nature Publishing Group. (d) At 80 K, circularly polarized photoluminescence (PL) spectra of *R*-MBA and *S*-MBA under excitation of 405 nm. Inset maps are the calculated energy band structures of *R*- and *S*-MBA, respectively. (f) At 80 K, circularly polarized PL spectra of *R*-/*S*-MBA alone, PEA/*R*-MBA, and PEA/*S*-MBA heterojunctions under excitation of 532 nm. (g) Schematics of the charge transfer process in PEA/*R*-MBA and PEA/*S*-MBA heterojunctions. Reproduced with permission from ref. 97. Copyright 2022, American Chemical Society.

doped PEPI. The CPL may be generated from the following two conditions: (1) the two dark exciton spin-state rates differ and are proportional to the relative arrangement between the Mn and the exciton spins. In the process of recombination, the imbalance of the spin state population can lead to CPL.[101] (2) The Mn spin-flipping simultaneously adopts a forbidden transition during the exciton recombination process. Additional radiation paths are provided by the Mn spin as well as the dangling bond spin. When the Mn spin is aligned in the external magnetic field, this path is more efficient for the exciton spin state, thus further generating the CPL.[102] In a word, manganese doping is a powerful approach to the control of exciton spin physics in RP-type perovskites. Non-magnetic MHPs are widely studied, while studies on magnetic MHPs are rare. We hope that prospective research could focus on regulating the spin electrons of MHPs, which will provide more spin properties for the development of MHP without chiral organic ligand materials.[103,104]

3.2. Chirality-controlled energy transfer

3.2.1. Upconversion-induced fluorescence strategy. A large g_{lum} value is one of the important parameters to achieve efficient CPL. Unluckily, inorganic materials often have a small g_{lum}.[105] Hence, the development of new strategies to achieve amplified g_{lum} is crucial. Based on the chiral and energy transfer,[81,106] it is evidenced that upconversion-induced fluorescence[36] and dry transfer stacking techniques are effective strategies to amplify g_{lum}.[40]

The upconversion-induced fluorescence[107] represents two molecules or atoms in the triplet state through mutual collision resulting in the formation of a molecule or an atom in the excited state and a molecule and an atom in the ground state. In the process, high-energy photons with high-energy emission could be achieved by the transformation of low-energy photons with low-energy excitation. Duan *et al.* tried to embed upconverted nanoparticles (UCNP) into perovskite nanocrystals (PKNC) to construct a novel UC-CPL active nanomaterial.[36] Scanning electron microscopy (SEM) confirmed that UCNP was successfully distributed inside PKNC, which in turn proved that the location of the UCNP luminescence peak matched the location of PKNC's exciton absorption peak. This proof also supported low-energy photons transferred from UCNP to PKNC producing high-energy photons. Chiral PKNC enables reabsorption of UCNP-generated chirality energy. Ultimately, the resulting CP degree of UC-CPL active material was amplified four times higher than the original PKNC,[37] and the g_{PL} value is amplified from 10^{-3} to 10^{-2}. An upconversion-induced fluorescence strategy provides an in-depth understanding of the chiral energy transfer mechanisms of nanocrystalline systems. From the above discussions, it provides a reference for a wide range of designed functionalized chiral inorganic nanocrystalline materials.[39] The pursuit of large g_{lum} values is an urgent challenge in the UC-CPL field. As a quasi-one-dimensional photonic crystal, nematic liquid crystals (N☆LC) have unique optical properties such as optical rotation and CD, making N☆LC an excellent substrate for achieving CPL with large g_{lum} values.[108] Generally, the doping of chiral compounds into achiral N☆LC is the preferred method to achieve N☆LC. Furthermore, changing the ratio of chiral dopants can flexibly adjust the photon band gap of N☆LC. In 2020, Duan *et al.* mixed the appropriate amount of $CsPbBr_3$-PKNC and UCNP in the N☆LC.[36] In this system, $CsPbBr_3$-PKNC and UCNP are used as energy acceptors and donors, respectively. It is well known

that the emission of the mixed emitters can be enhanced when $CsPbBr_3$-PKNC and UCNP are located at the edge of the photonic band gap, while that at the center of the photonic band gap will be suppressed. In addition, UCNP was given weaker emission after applying the electric field, and the UC-CPL emission can be switched off (Fig. 2e and f).

3.2.2. Dry transfer stacking technology. Based on the chiral energy transfer effect, constructing a perovskite heterojunction is a classical strategy without introducing chiral organic ligand molecules. For instance, Zhan *et al.* stacked the achiral $PEA_2MAPb_2I_7$ perovskite and chiral $(R\text{-}/S\text{-MBA})_2PbI_4$ perovskite to construct the $PEA_2MAPb_2I_7/[(R\text{-}/S\text{-MBA})_2PbI_4]$ perovskite heterojunction.[40,97] It is also known as a simple and versatile dry transfer stacking technique. In the structure of this perovskite heterojunction, the spiral axis of the chiral *R*-/*S*-MBA molecule is perpendicular to the planar PEA molecular sheet and parallel to the charge transfer direction, which is conducive to injecting charges. In this process, achieving a non-equilibrium spin population could adopt a achiral $PEA_2MAPb_2I_7$ perovskite to accept the spinning electrons of chiral $(R\text{-}/S\text{-MBA})_2PbI_4$ perovskite (Fig. 3g). Besides, to explore the effects of different excitation wavelengths on the CP degree of heterojunctions, the authors used excitation lights of 374, 405, and 532 nm wavelengths to excite the $PEA_2MAPb_2I_7/[(R\text{-}/S\text{-MBA})_2PbI_4]$ perovskite heterojunction, and obtained CP degrees of −6.1% (7.1%), −8.1% (8.9%) and −12.4% (13.8%), respectively (Fig. 3d and f). This means that switching the CPL signal is achieved by varying the excitation wavelength, which plays an important role in smart CPL switches for future applications. In summary, utilizing dry transfer stacking technology can stimulate the CP effect of achiral perovskite, and finally achieve robust and adjustable CPL materials.

3.3. Spin-relaxation-dynamic for circular polarization

In 2018, Sheng *et al.* first observed that circularly polarized light of different wavelengths excited the same achiral perovskite producing various CP degrees.[109] This study was carried out without an external magnetic field. At 77 K, circularly polarized light closes to 540 nm wavelength to excite $MAPbBr_3$, which is close to the exciton absorption peak located at 532 nm of $MAPbBr_3$. Then $MAPbBr_3$ produced CPL with a 2% CP degree. When circularly polarized light of 447 nm excited $MAPbBr_3$, the CP degree of $MAPbBr_3$ decreased to 0.3%. We can infer that using 447 nm circularly polarized light to excite $MAPbBr_3$ produces a decrease in the CP degree by an order of magnitude, compared to excitation at 532 nm circular polarized light. This result is attributed to the thermal relaxation[110] which was reflected in an order-of-magnitude reduction in the spin life of $MAPbBr_3$ excitons. Specifically, using 447 nm circularly polarized light to excite $MAPbBr_3$ produces non-resonant excitation and is insensitive to excitation photon energy. Meanwhile, the authors also explored the effect of temperature changes on the CP degrees of $MAPbBr_3$. When the temperature rises from 77 K to 110 K, authors measured the CP degrees of $MAPbBr_3$ by steady-state and referred to the Hanle effect.[111] The authors speculated that the spin life of $MAPbBr_3$ is unexpectedly longer about 240 ps at 77 K due to the large SOC. However, when the temperature rises to 110 K, the spin life is reduced by an order of magnitude. The authors added a magnetic field in a specific direction of the atoms and circularly polarized light-excited atoms, and the measured result indicates that atoms emit light showing a gradual decrease in CP degree ligands.

Theoretically, the heavy elements (Pb, I, and Br) in MHPs determine the electronic structure of perovskite edges, leading to perovskites with a large SOC.[112,113] Accordingly, the Rashba-type splitting effect can be attributed to the large SOC of perovskites and some phases lack reverse symmetry.[114] Consequently, Sheng *et al.* proposed that the spin life of excitons coexisting with large SOCs has great potential and needs further study. Related literature suggests that perovskites possess the larger SOC required for self-selective injection.[38] Nevertheless, the larger SOC of perovskites severely limits the spin relaxation lifetime.[38] However, study of the spin phenomena in MHPs is very limited. Fortunately, spin polarizers interact with each other like a pseudo-magnetic field. Therefore, the degraded spin state is improved, so that circularly polarized light-excited $MAPbBr_3$ induces the production of CD.[116]

In recent years, several studies have indicated that MHPs have Rashba effects.[117,118] For symmetry-breaking systems, a potential gradient existed at the surface/interface. Meanwhile, SOC leads to energy band cleavage, producing a pair of spin-momentum locked and spin-chiral opposite energy band structures. Notably, SOC is a bridge between spin electrons and orbitals interactions.[119] SOC provides the possibility of using external electric fields to modulate the orbital motion of electrons thereby regulating the spin state of electrons. Spin is an inherently quantum mechanical property of elementary particles, including electrons. Spin is closely related to the electronic and optical properties of materials.[120] Spins contain two types: one is the intrinsic spin for strong SOC, and the other is the non-intrinsic spin containing unpaired electrons with suspended bonds or chemical doping.

Low-temperature treated $MAPbI_3$ shows great potential in the field of luminescence and photovoltaics. $MAPbI_3$ has a large SOC. Hence, it can be inferred to have the performance of spin applications. In an earlier study, $MAPbI_3$ would have a direct band gap at the *R* point in the absence of the SOC, which is composed of six-fold degenerate $J = 1/2$ and $3/2$ ($L = 1$) guide bands (CBs) and double degenerate $J = 1/2$ ($L = 0$) high-valence bands (VBs) (Fig. 4c).[38,120] However, in the absence of a SOC, the CB is divided into a lower double degeneracy $J = 1/2$ and a higher quadruple degenerate state $J = 3/2$ band. Here, the authors focused the study on near-band gap excitation. In addition, using circular pump–probe measurements, the authors demonstrated that highly polarized electrons with a total angular momentum (J) of ~90% can be photogenerated in perovskite according to circular pump–probe measurements (Fig. 4a and b). Meanwhile, spin relaxation in $MAPbI_3$ occurs by J flipping. The authors elucidated the electron spin relaxation lifetime to be ~7 ps and that of the hole is ~1 ps by a simple two-state model. This work shows the potential of $MAPbI_3$ as a new candidate for spintronics applications, especially acting as

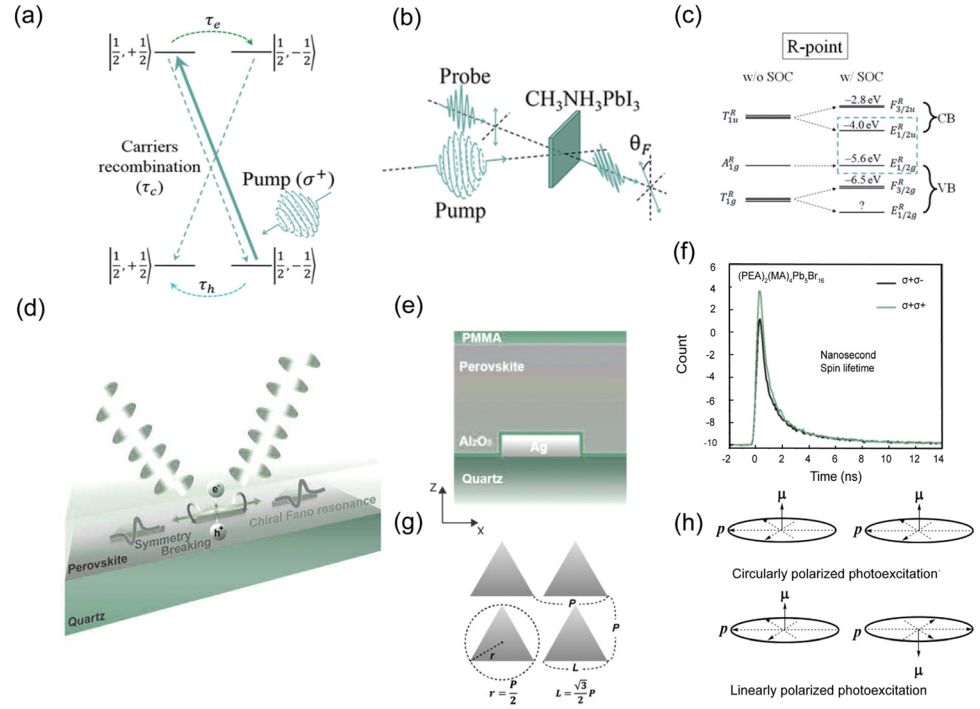

Fig. 4 (a) Model of near band-edge photoexcitation by σ^+ photon and J-state dynamics of $CH_3NH_3PbI_3$. $|J,m_J\rangle$ stands for the state notation, where J = 1/2 is the electron's total angular momentum quantum number and $m_J = \pm 1/2$ is its projection in the z-axis. (b) The diagrammatic sketch of circular pump–probe measurements of $CH_3NH_3PbI_3$. (c) The R-point represents point group symmetry representation. Energy bands of $CH_3NH_3PbI_3$ at the R-point with their respective levels from the vacuum (experimental). The dashed box indicates the bands of interest. Reproduced with permission from ref. 38. Copyright 2015, American Chemical Society. (d) Schematic for circularly polarized emission based on chiral Fano resonances. (e) Schematic for the sample, where $MAPbI_3$ is spin-coated on top of a symmetry-broken structure (triangular silver patterns, thickness ~40 nm). Reproduced with permission from ref. 41. Copyright 2021, American Chemical Society. (f) The PL circular polarization ($\sigma^+\sigma^+ - \sigma^+\sigma^-$) of quasi-2D perovskite [$(PEA)_2(MA)_4Pb_5Br_{16}$ with n = 5]. Reproduced with permission from ref. 115. Copyright 2020, American Chemical Society. (g) A triangular pattern is designed to have a distance r (from the triangle center to the triangle vertex) to be $P/2$, where P is the period of silver patterns. The side length L of triangular patterns is ~350 nm. Reproduced with permission from ref. 41. Copyright 2021, American Chemical Society. (h) Orbital polarization and magnetic dipoles are generated between excited states by circularly and linearly polarized photoexcitations. Reproduced with permission from ref. 115. Copyright 2020, American Chemical Society.

ultrafast spin switches. However, solution-treated $MAPbI_3$ films for spin transport purposes have some limitations, but it is still possible to overcome these drawbacks by improving the fabrication techniques of the sample (*e.g.*, vacuum deposition).

It can be inferred that by introducing a spin into $MAPbI_3$ perovskite at room temperature the spin–orbit coupling phenomenon can be observed at the ferromagnet/perovskite interface,[121] which has aroused people's interest in spintronics. From the above discussions, it is conducive to the convenient adjustment of spin parameters by adjusting electrical parameters.

4. Circularly polarized light-emitting devices

4.1. Photoluminescent devices

In general, because crystals are anisotropic, they are prone to emit linearly polarized light. Correspondingly, a CPL material is more likely to have a spiral structure. It is more difficult to obtain a material with a spiral structure than to obtain a uniaxial structure.

In 2019, Li *et al.* successfully prepared a chiral cholesteric liquid crystal (CLC) superstructure stack and obtained full-color CPL.[122] The preparation was performed as follows: two CLC membranes with opposite helical structures served as filters and were sandwiched between layers of perovskite NCs to self-assemble into a chiral CLC superstructure stack. Further modulating the dissymmetry of the nanomaterials could achieve full CPL *via* offsetting the reflection and emission band overlap. This method enables non-polarized light emissions of the originally inorganic perovskite NCs to converse to fully CPL with $g_{lum} \sim 1.6$. The specific working principle of CLC superstructure stacking is as follows: once the perovskite NCs film is stacked on the R-CLC film that overlaps the perovskite NCs film emission spectrum, half of the downward emitted light is reflected by the R-CLC film and the electric field film. In particular, the downward luminescence is defined as left-handed, owing to the presence of a helical structure in the emitted light with the same shape as the cholesteric helix shape. Here a 180° phase shift occurs and a chiral transition takes place. While the upward emitted light is defined as constant right-handed light. In principle, the 1D helical cholesteric superstructure is capable of achieving a 100% circularly polarized conversion efficiency.

Compared to previous approaches, the chiral CLC superstructure stacking strategy is more straightforward and powerful and can achieve full-color chiral luminescence. It also offers new opportunities for optoelectronic and photonic devices.

Notably, the g_{lum} values of the perovskite-based CPL are just on the order of 10^{-3} to 10^{-2}, much lower than the theoretical maxima g_{lum} value of 2.0.[123] This seriously hinders the utility of the CPL. In 2022, Liu *et al.* constructed bilayer structured devices by embedding $MAPbBr_3$ NCs into a polymer matrix and coupled $MAPbBr_3$ NCs with a stimuli-responsible soft helix (chiral liquid crystals).[61] The g_{lum} value of the constructed bilayer structured devices up to 1.9 and a robust CPL was obtained. In the process of fabrication, they considered that the polymer matrix limits the self-aggregation of perovskite NCs and protects them from oxygen and polar molecules. Then, they compared the characterization of $MAPbBr_3$ nanocrystalline-embedded commercially available polyvinyl polymers films, such as PAN, polyvinylidene fluoride (PVDF) and polyvinyl pyridine (PVP). XRD testing suggests an enhanced crystallization of perovskite NCs in PAN film relative to other polymers. Based on X-ray photoelectron spectroscopy (XPS) testing, Pb 4f peaks shift to lower binding energies by 1.3, 0.8, and 0.2 eV in the PAN^{-}, $PVDF^{-}$, and PVP-based film that suggests a stronger coordination of PAN to Pb^{2+}. It also shows that PVP effectively passivated the surface defects of perovskite NCs, leading to high PLQY production and reduced non-radiative recombination. Among the three polymers, PAN is the best polymer matrix to ensure the high emission of $MAPbBr_3$ NCs, which not only enhances the emittance but also significantly improves the stability of perovskite emitters in a polar environment.

Spin-polarized excitons have long radiation recombination times of nanosecond scale and spin relaxation times of picosecond scale. CP at room temperature is often limited to a few percentage points. Therefore, achieving high CP at room temperature is extremely challenging. In 2021, Young Chul Jun *et al.* spun $MAPbI_3$ and $MAPbBr_3$ perovskites active layers onto a silver triangle pattern,[41] which has a small size of $\sim$350 nm and a symmetrical fracture structure (Fig. 4d, e and g). This process avoids the patterning of perovskite layers, as patterned perovskite layers can damage the fragile luminescent active layer. At room temperature, there is a phenomenon that the narrow-mode position of chiral Fano resonance was strongly enhanced by a large range of CP degrees over 0.5. The essence of chiral Fano resonance is triggered by the symmetrical breaking-induced chiral response in the plate mode. In addition, the chiral Fano resonance manifestation is the difference between the reflection spectrum and the PL spectrum position.[41] The reciprocity calculation shows that under the light incidence of RCP and LCP, the narrow mode position of chiral Fano resonance causes a huge difference in the field strength of RCP and LCP. Accordingly, the reverse propagation mode of RCP and LCP emission directional coupling increases the helicity of the material. It not only protects the excellent photoelectric properties of perovskites but also achieves a large range of CP greater than 0.5 at room temperature. It is expected that the symmetrical broken patterned substrate will be combined with various perovskite materials in the future. This work looks forward to the application prospect of Chiral Fano Resonance[124] for the light source generating CPL so that the emission wavelength is controlled in the visible light range.

4.2. Electroluminescent devices

It is well known that achieving spin polarization often requires an applied magnetic field. Luckily, Kim *et al.* displayed a spin-polarized light-emitting diode (LED) relying on the CISS effect.[43] In terms of the operation mechanism, spin holes are injected into the active layer without applying a magnetic field and ferromagnetic contact at room temperature. In this process, spin dephasing is inhibited in the emission layer, and the accumulation of carrier charges is also inhibited in the spin interface. Notably, a chiral 2D $[(R/S\text{-MBA})_2PbI_4]$ (n = 1) perovskite layer with a thickness of 30–60 nm could increase the CISS effect, which served as a spin filter and determines the spin direction. The chiral organic ammonium *R*/*S*-MBA spiral axis is perpendicular to the $CsPbI_3$ NCs light-emitting layer so that it is parallel to the direction of charge transfer. This facilitates the transfer of spintronics. Hence, it is easy to produce correct holes–electrons recombination through the $(R/S\text{-MBA})_2PbI_4$ layer injecting holes and $CsPbI_3$ NCs emitting layer injecting electrons. The final prepared spin-polarized LED at room temperature achieved $\pm$2.6% circular polarized electroluminescence efficiency.[43]

Aimed at the CISS effect, injecting the spin holes can suppress spin dephasing in the emission layer. Hu *et al.* systematically investigated the factors affecting the spin dephasing in the emission layer.[115] When linear polarization light transfers into circular polarization light, the PL of excited quasi-2D (n = 5) perovskite exhibits positive values (Fig. 4h). This proves that orbital polarization in the excited state creates long-range orbital–orbital interactions. When the short-range orbital–orbital interaction dominates between orbital magnetic dipoles and the light excitation transfer from linear polarization to circular polarization luminescence, PL exhibits negative values, indicating that an interaction occurs between the orbitals of the excited dipoles. Circularly polarized light-excited quasi-2D (n = 5) perovskites produce orbital magnetic dipoles in the same direction between the excited states. However, linear polarization excited quasi-2D (n = 5) perovskite produces orbital magnetic dipoles in the opposite direction. Therefore, circularly polarized light excitation produces a stronger total orbital magnetic dipole momentum than linearly polarized light excitation. Besides circularly polarized light excitation leads to a greater spin flip, thus converting the spin allowable state into a spin inhibited state. Herein, a lower PL intensity emerges. We can conclude that long-range and short-range orbital–orbital interactions are the main factors that control the spin kinetics of the luminescent state in mixed-phase perovskites. However, spin life is not detected in 2D/3D perovskite films, demonstrating that magnetic dipole interactions of short-range orbital–orbital are major causes of spin dephasing in excited states.[115]

In 2022, Xiao *et al.* confirmed that the chiral 2D $(S\text{-}/R\text{-MBA})_2PbI_4$ shell layer as a spin filter can inject spinning electrons into

the achiral $MAPbBr_3$ core layer (Fig. 5d).[127] Considering that organic materials are full of weak SOC and ultrafine interaction characteristics, generally speaking, organic materials do not have an effective spin relaxation mechanism and the spin lifetime tends to be longer. Consequently, $MAPbBr_3$ perovskite was chosen as the core layer. Based on the CISS effect, achieving spin-dependent polarized electron injection from the chiral (*S*/*R*)-PEA (OA) NCs shell layer to achiral $MAPbBr_3$ core NCs. Subsequently, the spin polarization distribution of the holes appeared in the valence band of the $MAPbBr_3$ core layer, then the conduction band electrons and the valence band holes undergo recombination at the $MAPbBr_3$ core layer (Fig. 5c). Afterward, the electron–hole complex is defined as a clear spin state and triggers the $MAPbBr_3$ core layer to act as an excitation band of the CPL. This process is dependent on polarization and no chiral transfer occurs. Moreover, there are no sacrifices of structural symmetry and luminescence characteristics based on the CISS effect. Besides, the electrons' orientation can be linked to molecular symmetry. The 3D $MAPbBr_3$@$(S$-/R-$MBA)_2PbI_4$ core–shell structure finally achieved a dissymmetry circularly polarized electroluminescence (CPEL) factor ($g_{CP\text{-}EL} = 6 \times 10^{-3}$), PLQY = 54%, and a maximum $|g_{lum}| = 4.0 \times 10^{-3}$ at room temperature. g_{lum} can be indicated as an equation: $g_{lum} = 2 \times (I_L - I_R)/(I_L + I_R)$, where I_L and I_R are the intensity of left and right CPL, accordingly (Fig. 5e and f). This achievement will have great research potential in spintronics and optoelectronics.[125]

The Hamiltonian algorithm can represent the SOC energy shift and the hyperfine interaction strength, where the atomic number of the material is represented by Z.[128] According to eqn (4) and (5), the prepared chiral organic ammonium MHPs with small Z-values have smaller SOC and hyperfine interaction strength.[129] In this regard, it can be concluded that the chiral organic ammonium MHPs with small Z-value have longer spin lifetimes and are more favorable for spin-polarization transfer.

$$\left\langle H_{SO,n,j=l\pm\frac{1}{2},l} \right\rangle = \frac{mc^2(Z\alpha)^4}{4n^3 l\left(l+\frac{1}{2}\right)(l+1)} \begin{pmatrix} l \\ -l-1 \end{pmatrix}; \quad l \geq 1 \quad (4)$$

$$\langle H_{hyp} \rangle_{n,\frac{1}{2},0} = \frac{4g_N m^2 (Z\alpha)^4 SI}{3M_N n^3 h^2} \quad (5)$$

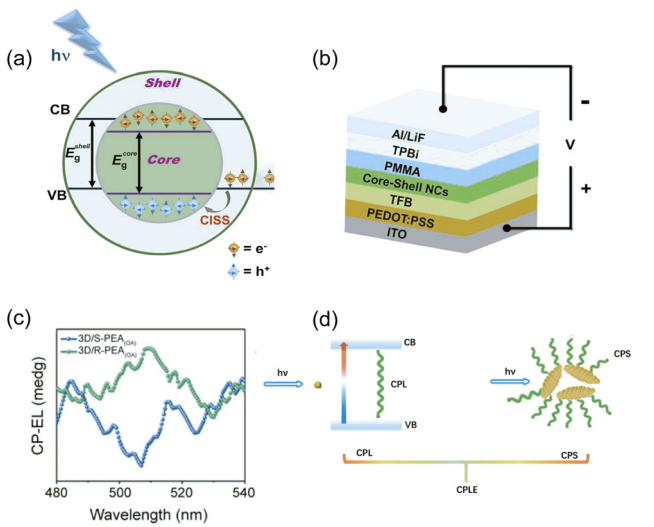

Fig. 5 (a) Schematic illustration of spin-polarized electron generation in the core–shell NCs. (b) The device structure of the spin-LEDs is based on 3D/*S*(*R*)-$PEA_{(OA)}$ NCs with the 4 : 6 molar ratio of the shell and core. (c) The CP-EL of spin-LED based on 3D/*S*(*R*)-PEA(OA) perovskites NCs. Reproduced with permission from ref. 125. Copyright 2022, American Chemical Society. (d) A schematic illustration of the physical mechanism of CPL (left) and CPS (right). Reproduced with permission from ref. 126. Copyright 2022, Wiley-VCH.

5. Perspective and prospect

5.1. In materials

Compared with 0D, 1D, and 2D (n = 1) perovskites with large organic ammonium cationic volume, the cubic octahedron of 3D perovskites has a small cavity. For 3D perovskites, the cation radius of the cavity content is relatively strict, and it is impossible to accommodate cations other than Cs^+, FA^+, and MA^+. For 2D (n = 1) perovskite, the proportion of the chiral organic ammonium to the total components is higher than that of dimension-reduced perovskite ($n \geq 2$). Hence, the CPL signal of 2D (n = 1) perovskite is stronger. Currently, CPL-related research is mainly concentrated in 0D, 1D, and 2D (n = 1) perovskites. However, 3D perovskites possess additional special properties such as longer carrier lifetimes and smaller exciton binding energy. Theoretical calculations predict the stable existence of chiral 3D perovskites, so the development of chiral 3D perovskites is also very important.[130] It can be concluded that the structure, modification, and composition of the material play key roles in the CPL characteristics of MHP materials.

The achievement of CPL with high CD intensity and high g_{lum} values by screening systematically chiral organic ammonium cations. The modulation of CD intensity can be correlated to the varied magnetic transition dipole of different chiral organic ligands incorporated into perovskites. Notably, the rotational strength of chiral HOIPs can theoretically be determined by the scalar product between the electric transition dipole moment ($M_{(elec.\ dipole)}$ electric dipole) and the magnetic transition dipole moment ($M_{(Mag.\ dipole)}$) (eqn (6))[30] in which R_{theo} is the rotatory strength. In addition, R_{theo} is directly proportional to the CD signal intensity. R_{theo} is lower, and the higher CPLE intensity is often unattainable. We can conclude that the intensity of CD and CPL signals can be controlled by systematic chiral organic cations. Therefore, it is crucial to develop amplifying chiral signals *via* composition tuning strategies. For MHP materials, a common strategy is to introduce chiral organic ammonium cations to break the original structural symmetry of MHPs to achieve chiral transfer. At the same time, when mixed halogen ions are tuned to the iodine-predominant phase and bromine-dominated phase, the CD signal can produce "turn on" and "turn off" signals, respectively and regulate the wavelength of CD by modulating the exciton band structure.

In addition, the feeding ratio of the raw materials controls the dimension, and adding a small number of additives controls the quality of the crystallinity. This could all affect the intensity of the CD signal. CPL materials are often limited to introducing a chiral organic to MHPs. Based on perovskites with greater SOC characteristics and CISS effects, for achiral organic ammonium MHPs materials, the development of new strategies such as regulating spin electrons, upconversion-induced fluorescence, and chiral energy transfer.[97,131] New strategies need to be developed as a breakthrough point to improve the low $|g_{CPL}|$ and low CD intensity of MHP materials.

$$R_{theo} = \frac{1}{2mc} Im \int \varphi_g \hat{M}_{(elec.\ dipole)} \varphi_e d\tau \int \varphi_g \hat{M}_{(mag.\ dipole)} \varphi_e d\tau \quad (6)$$

Based on the consideration of environmental friendliness, there is an urgent need to develop non-toxic, stable, and high-performance MHP materials with CPL. The toxicity and damp heat of Pb-based perovskite hinder the development of CPL-emitting devices. Sn-based perovskites are defined as alternative Pb-based perovskites. However, the oxidation of Sn-based perovskites limits the further development of MHP properties.[132]

5.2. New design strategies to amplify CD signals

Drawing on chiral amplification strategies plays an important role in the development of chiral MHPs. The asymmetric emission of small organic molecules can change a series of technologies such as communication and display. In fact, as for individual organic small molecules, high CPL emission is usually not possible. Interestingly, in 2021, Fuchter *et al.* investigated whether amplification of the chiral signal is not only influenced by chiral environmental effects but is also triggered by the electric coupling of the electric and magnetic transition dipoles.[52] Subsequently, the circularly polarized Förster resonance energy transfer effect appeared between the conjugated polymer donor and the p-type helicene acceptor. After the coupling action of the electro-jumping dipole, the generation of CP Förster resonance energy transfer could also amplify the chiral CD signal intensity. The method is applicable to enhancing the *g*-factor of simple organic small molecules. The final result demonstrates that introducing the donor to a polymer system produces a nearly 10^3-fold amplification of the CD signal intensity, compared to the system without the introduction of the donor. This work provides a general strategy for chiral emitters of intrinsically asymmetric small molecules.

5.3. In optics

Optics also have the Rashba effect, manifested as a split of optical states with opposite chirality in momentum space. The helix of light polarization represents the spin freedom of the SOC. Tian *et al.* developed a Rashba effect-based optical device split in the momentum space that can support the chiral emission source.[133] Specifically, directly imprinting medium with a destructive surface characteristic of symmetry breaking in the layer of $MAPbI_3$ perovskite film. Directly imprinting MHPs achieves a CP degree of ±60% and their CP intensity is 6 times that of perovskite without imprinting. Moreover, compared with the solution synthesis method, the direct imprinting method can be applied for large-area patterning of perovskites. The study demonstrated the existence of optical Rashba splitting on the in-plane operative $MAPbI_3$ subsurface. In the meantime, this discovery will lead to the development of planar light-emitting nanodevices. It has potential future applications in holography, biosensing, encoding, and quantum optics. In principle, both differential absorption and differential scattering of circularly polarized emission from nanostructures contribute to the formation of CD signals.

When light passes through a light-emitting chiral medium containing nanoscale components, there will be circularly polarized luminescence (CPL) and circularly polarized scattering (CPS).[126] Therefore, circularly polarized light emission (CPLE) carries the cumulative effect of both CPL and CPS, which is the polarized net flux of photons leaving the optically active medium. As is shown in Fig. 5f, CPS refers to the interaction of light with nanostructures to produce a scattering of left- and right-handed light. Except for the scattered absorption band, only differential scattering by chiral particles contributes to CD. The scattering of the sample depends on the angle between the incident beam and the scattered beam. Except for the angles of 0° and 180° between the incident beam and the scattered beam, the beam is not circularly polarized. When a left circularly polarized beam is incident on a point scatterer, the scattered light consists of left circularly polarized light at 0°, linear polarized light at 90°, and right circular polarized light at 180°. Except for the above three angles, the produced light is in an elliptically polarized state depending only on the angle between the incident beam and the scattered beam. In addition to this, the periodic variation of the refractive index of the material may lead to Bragg scattering of photons. Here, achiral cholesteric materials emit circularly polarized light generated by CPS. Notably, for particle sizes are greater than 1/20 of the light wavelength, differential scattering plays a crucial role. In addition, for nano-molecules with sizes that are much smaller than the emission wavelength, circularly polarized Raleigh scattering is produced, which contributes to the formation of circularly polarized emission.[44] For Raleigh scattering,[134] it is not only on the geometry of the NCs lattice but also on the dissymmetry of the optical constants. Consequently, the chirality, shape, and orientation of the emitting particles affect the ellipticity, wavelength, and intensity of the CPS. Assuming that the nonlinear processes of second-order Raleigh scattering and circularly polarized Mie scattering are neglected, CPL dominates the CPLE materials including organic complexes, nanoclusters, nanostructured semiconductors, and chalcogenides. Correspondingly, CPS[135] dominates the CPLE material in AuAg bimetallic nanoclusters,[136] which are self-assembled with a guanosine 5′-monophosphate chiral template into a helical structure. The helical structure is provided with a width of 200 nm and several micrometers in length. Then strong light scattering appeared and showed CPL properties. Furthermore, the self-assembled nanomaterials were adjusted by alkali metal ions to obtain the maximum $|g_{PL}|$ value of 2.7×10^{-2}. Additionally, other studies have recently demonstrated

that CPS-leading circularly polarized light emission can obtain more desirable $|g_{PL}|$ values.[137]

In summary, for many nanostructured optical media, CPS is an important component of circularly polarized light emission.[138,139] This provides new insight and strategy for the development of new circularly polarized light emission materials as well as new circularly polarized light emission electroluminescence materials. At present, the distinction between the contribution of CPL and CPS to circularly polarized light emission is unresolved. Investigating the reason, small changes in the chemistry of the nanomaterials and the preparation of sample films, can all significantly alter the contribution of CPL and CPS. From the above discussions, we can conclude that realizing strong CD signal intensity can be achieved by tuning the balance of CPL and CPS.

5.4. Integration and arrays

The research of chiral perovskite nanomaterials is still in the early stages of development. In the future, CPL devices will overcome barriers to performance optimization, device integration, and arrays. Compared with polycrystalline perovskite thin films, single-crystal perovskites have no grain boundaries, the charge trap state density is the smallest and they have higher charge-carrier mobility. Single-crystal perovskite is the best choice for array structures. Fabricating large-scale, high-resolution single-crystal perovskite arrays with ideal morphology and size remains a challenge. Perovskite arrays will potentially revolutionize technology applications and facilitate the development of such integrated optoelectronic and photonic devices.

Author contributions

M. Y. conceived the idea. M. Y. guided the Perspective. B. L. organized the pictures. B. L., L. Z., Y. J., and S. C. contributed to the manuscript. All authors discussed the results and commented on the manuscript.

Conflicts of interest

There are no conflicts to declare.

Acknowledgements

This work is financially supported by the National Key Research and Development Program of China (2022YFE0201500). M. Yuan acknowledges financial support from the National Natural Science Foundation of China (No. 62261160389 and T2225024).

Notes and references

1 T. Ishihara, J. Takahashi and T. Goto, *Phys. Rev. B: Condens. Matter Mater. Phys.*, 1990, **42**, 11099.
2 C. R. Kagan, D. B. Mitzi and C. D. Dimitrakopoulos, *Science*, 1999, **286**, 945–947.
3 M. Yuan, L. N. Quan, R. Comin, G. Walters, R. Sabatini, O. Voznyy, S. Hoogland, Y. Zhao, E. M. Beauregard and P. Kanjanaboos, *Nat. Nanotechnol.*, 2016, **11**, 872–877.
4 G. Long, C. Jiang, R. Sabatini, Z. Yang, M. Wei, L. N. Quan, Q. Liang, A. Rasmita, M. Askerka and G. Walters, *Nat. Photonics*, 2018, **12**, 528–533.
5 Z. N. Georgieva, B. P. Bloom, S. Ghosh and D. H. Waldeck, *Adv. Mater.*, 2018, **30**, 1800097.
6 Y. Dong, Y. Zhang, X. Li, Y. Feng, H. Zhang and J. Xu, *Small*, 2019, **15**, 1902237.
7 Z. N. Georgieva, B. P. Bloom, S. Ghosh and D. H. Waldeck, *Adv. Mater.*, 2018, **30**, 1800097.
8 D. Niesner, M. Wilhelm, I. Levchuk, A. Osvet, S. Shrestha, M. Batentschuk, C. Brabec and T. Fauster, *Phys. Rev. Lett.*, 2016, **117**, 126401.
9 J. Even, L. Pedesseau, J.-M. Jancu and C. Katan, *J. Phys. Chem. Lett.*, 2013, **4**, 2999–3005.
10 X. Yang, X.-M. Li, Y. Li, Y. Li, R. Sun, J.-N. Liu, X. Bai, N. Li, Z.-K. Xie and L. Su, *Nano Lett.*, 2020, **21**, 77–83.
11 R. Farshchi, M. Ramsteiner, J. Herfort, A. Tahraoui and H. Grahn, *Appl. Phys. Lett.*, 2011, **98**, 162508.
12 D. Fu, J. Xin, Y. He, S. Wu, X. Zhang, X. M. Zhang and J. Luo, *Angew. Chem., Int. Ed.*, 2021, **60**, 20021–20026.
13 W. Dai, Y. Wang, R. Li, Y. Fan, G. Qu, Y. Wu, Q. Song, J. Han and S. Xiao, *ACS Nano*, 2020, **14**, 17063–17070.
14 L. Barron, *Chem. Soc. Rev.*, 1986, **15**, 189–223.
15 D. Di Nuzzo, L. Cui, J. L. Greenfield, B. Zhao, R. H. Friend and S. C. Meskers, *ACS Nano*, 2020, **14**, 7610–7616.
16 J. Young, P. Lalkiya and J. M. Rondinelli, *J. Mater. Chem. C*, 2016, **4**, 4016–4027.
17 T. Goto, Y. Okazaki, M. Ueki, Y. Kuwahara, M. Takafuji, R. Oda and H. Ihara, *Angew. Chem., Int. Ed.*, 2017, **56**, 2989–2993.
18 E. M. Sánchez-Carnerero, A. R. Agarrabeitia, F. Moreno, B. L. Maroto, G. Muller, M. J. Ortiz and S. de la Moya, *Chem. – Eur. J.*, 2015, **21**, 13488–13500.
19 D. G. Billing and A. Lemmerer, *Acta Crystallogr., Sect. E: Struct. Rep. Online*, 2003, **59**, 381–383.
20 D. G. Billing and A. Lemmerer, *CrystEngComm*, 2006, **8**, 686–695.
21 J. Bie, D.-B. Yang, M.-G. Ju, Q. Pan, Y.-M. You, W. Fa, X. C. Zeng and S. Chen, *JACS Au*, 2021, **1**, 475–483.
22 L.-S. Li, Y.-H. Tan, W.-J. Wei, H.-Q. Gao, Y.-Z. Tang and X.-B. Han, *ACS Appl. Mater. Interfaces*, 2020, **13**, 2044–2051.
23 Y. Shi, P. Duan, S. Huo, Y. Li and M. Liu, *Adv. Mater.*, 2018, **30**, 1705011.
24 G. Long, R. Sabatini, M. I. Saidaminov, G. Lakhwani, A. Rasmita, X. Liu, E. H. Sargent and W. Gao, *Nat. Rev. Mater.*, 2020, **5**, 423–439.
25 Q. Wei and Z. Ning, *ACS Mater. Lett.*, 2021, **3**, 1266–1275.
26 M. Linares, A. Minoia, P. Brocorens, D. Beljonne and R. Lazzaroni, *Chem. Soc. Rev.*, 2009, **38**, 806–816.
27 C. Zhou, Y. Chu, L. Ma, Y. Zhong, C. Wang, Y. Liu, H. Zhang, B. Wang, X. Feng and X. Yu, *Phys. Chem. Chem. Phys.*, 2020, **22**, 17299–17305.
28 M. Li, F. Fang, X. Huang, G. Liu, Z. Lai, Z. Chen, J. Hong, Y. Chen, R.-J. Wei and G.-H. Ning, *Chem. Mater.*, 2022, **34**, 2955–2962.

29 J. Ahn, S. Ma, J.-Y. Kim, J. Kyhm, W. Yang, J. A. Lim, N. A. Kotov and J. Moon, *J. Am. Chem. Soc.*, 2020, **142**, 4206–4212.
30 J. T. Lin, D. G. Chen, L. S. Yang, T. C. Lin, Y. H. Liu, Y. C. Chao, P. T. Chou and C. W. Chiu, *Angew. Chem., Int. Ed.*, 2021, **133**, 21604–21610.
31 A. Ishii and T. Miyasaka, *Sci. Adv.*, 2020, **6**, eabd3274.
32 D. Parobek, B. J. Roman, Y. Dong, H. Jin, E. Lee, M. Sheldon and D. H. Son, *Nano Lett.*, 2016, **16**, 7376–7380.
33 S. Rao, J. Srivastava, M. Wu, B. Mok, C. Chen, M. Ling, H.-L. Liu, Y. Chen and J. Ho, *J. Supercond. Novel Magn.*, 2011, **24**, 1249–1262.
34 S. Zou, G. Yang, T. Yang, D. Zhao, Z. Gan, W. Chen, H. Zhong, X. Wen, B. Jia and B. Zou, *J. Phys. Chem. Lett.*, 2018, **9**, 4878–4885.
35 T. Neumann, S. Feldmann, P. Moser, A. Delhomme, J. Zerhoch, T. Van De Goor, S. Wang, M. Dyksik, T. Winkler and J. J. Finley, *Nat. Commun.*, 2021, **12**, 1–8.
36 X. Yang, M. Zhou, Y. Wang and P. Duan, *Adv. Mater.*, 2020, **32**, 2000820.
37 T. Ogawa, N. Yanai, A. Monguzzi and N. Kimizuka, *Sci. Rep.*, 2015, **5**, 1–9.
38 D. Giovanni, H. Ma, J. Chua, M. Grätzel, R. Ramesh, S. Mhaisalkar, N. Mathews and T. C. Sum, *Nano Lett.*, 2015, **15**, 1553–1558.
39 X. Jin, M. Zhou, J. Han, B. Li, T. Zhang, S. Jiang and P. Duan, *Nano Res.*, 2022, **15**, 1047–1053.
40 S. Gangoli, A. Gutsol and A. Fridman, Rotating non-equilibrium gliding arc plasma disc for enhancement in ignition and combustion of hydrocarbon fuels, Proceedings of the 17th International Symposium on Plasma Chemistry, 2005.
41 I. C. Seo, Y. Lim, S.-C. An, B. H. Woo, S. Kim, J. G. Son, S. Yoo, Q.-H. Park, J. Y. Kim and Y. C. Jun, *ACS Nano*, 2021, **15**, 13781–13793.
42 R. Naaman and D. H. Waldeck, *J. Phys. Chem. Lett.*, 2012, **3**, 2178–2187.
43 Y.-H. Kim, Y. Zhai, H. Lu, X. Pan, C. Xiao, E. A. Gaulding, S. P. Harvey, J. J. Berry, Z. V. Vardeny and J. M. Luther, *Science*, 2021, **371**, 1129–1133.
44 C. Bustamante, I. Tinoco Jr and M. F. Maestre, *Proc. Natl. Acad. Sci. U. S. A.*, 1983, **80**, 3568–3572.
45 Z. N. Georgieva, Z. Zhang, P. Zhang, B. P. Bloom, D. N. Beratan and D. H. Waldeck, *J. Phys. Chem. C*, 2022, **126**, 15986–15995.
46 F. S. Richardson and J. P. Riehl, *Chem. Rev.*, 1977, **77**, 773–792.
47 D. P. Craig and T. Thirunamachandran, *Molecular quantum electrodynamics: an introduction to radiation-molecule interactions*, Courier Corporation, 1998.
48 B. Regan, E. D. Commins, C. J. Schmidt and D. DeMille, *Phys. Rev. Lett.*, 2002, **88**, 071805.
49 T. Feng, Y. Xu, W. Zhang and A. E. Miroshnichenko, *Phys. Rev. Lett.*, 2017, **118**, 173901.
50 T. Mori, *Circularly polarized luminescence of isolated small organic molecules*, Springer, Singapore, 2020.
51 H. Tanaka, Y. Inoue and T. Mori, *ChemPhotoChem*, 2018, **2**, 386–402.
52 J. Wade, J. R. Brandt, D. Reger, F. Zinna, K. Y. Amsharov, N. Jux, D. L. Andrews and M. J. Fuchter, *Angew. Chem., Int. Ed.*, 2021, **60**, 222–227.
53 J. R. Brandt, F. Salerno and M. J. Fuchter, *Nat. Rev. Chem.*, 2017, **1**, 1–12.
54 Y. Nagata and T. Mori, *Front. Chem.*, 2020, **8**, 448.
55 K. Ma, W. Chen, T. Jiao, X. Jin, Y. Sang, D. Yang, J. Zhou, M. Liu and P. Duan, *Chem. Sci.*, 2019, **10**, 6821–6827.
56 I. Z. Steinberg, *Annu. Rev. Biophys. Bioeng.*, 1978, **7**, 113–137.
57 C. Chen, L. Gao, W. Gao, C. Ge, X. Du, Z. Li, Y. Yang, G. Niu and J. Tang, *Nat. Commun.*, 2019, **10**, 1–7.
58 Y.-H. Kim, Y. Zhai, E. A. Gaulding, S. N. Habisreutinger, T. Moot, B. A. Rosales, H. Lu, A. Hazarika, R. Brunecky and L. M. Wheeler, *ACS Nano*, 2020, **14**, 8816–8825.
59 W. Chen, S. Zhang, M. Zhou, T. Zhao, X. Qin, X. Liu, M. Liu and P. Duan, *J. Phys. Chem. Lett.*, 2019, **10**, 3290–3295.
60 R. Cao, X. Yang, Y. Wang and Y. Xiao, *Nano Res.*, 2022, **16**, 1459–1464.
61 S. Liu, X. Liu, Y. Wu, D. Zhang, Y. Wu, H. Tian, Z. Zheng and W.-H. Zhu, *Matter*, 2022, **5**, 2319–2333.
62 H. Kim, S. W. Im, R. M. Kim, N. H. Cho, H.-E. Lee, H.-Y. Ahn and K. T. Nam, *Mater. Adv.*, 2020, **1**, 512–524.
63 Y. Li, T. Higaki, X. Du and R. Jin, *Adv. Mater.*, 2020, **32**, 1905488.
64 S. Ma, J. Ahn and J. Moon, *Adv. Mater.*, 2021, **33**, 2005760.
65 J. Ma, H. Wang and D. Li, *Adv. Mater.*, 2021, **33**, 2008785.
66 Y. Qin, F.-F. Gao, S. Qian, T.-M. Guo, Y.-J. Gong, Z.-G. Li, G.-D. Su, Y. Gao, W. Li and C. Jiang, *ACS Nano*, 2022, **16**, 3221–3230.
67 L. Zhang, C. Sun, T. He, Y. Jiang, J. Wei, Y. Huang and M. Yuan, *Light Sci. Appl.*, 2021, **10**, 1–26.
68 J. Ma, C. Fang, C. Chen, L. Jin, J. Wang, S. Wang, J. Tang and D. Li, *ACS Nano*, 2019, **13**, 3659–3665.
69 C. Chen, L. Gao, W. Gao, C. Ge, X. Du, Z. Li, Y. Yang, G. Niu and J. Tang, *Nat. Commun.*, 2019, **10**, 1–7.
70 S. D. Mahapatra, P. C. Mohapatra, A. I. Aria, G. Christie, Y. K. Mishra, S. Hofmann and V. K. Thakur, *Adv. Sci.*, 2021, **8**, 2100864.
71 S. A. Kulkarni, T. Baikie, P. P. Boix, N. Yantara, N. Mathews and S. Mhaisalkar, *J. Mater. Chem. A*, 2014, **2**, 9221–9225.
72 F. Hao, C. C. Stoumpos, R. P. Chang and M. G. Kanatzidis, *J. Am. Chem. Soc.*, 2014, **136**, 8094–8099.
73 R. Prasanna, A. Gold-Parker, T. Leijtens, B. Conings, A. Babayigit, H.-G. Boyen, M. F. Toney and M. D. McGehee, *J. Am. Chem. Soc.*, 2017, **139**, 11117–11124.
74 W. Chen, S. Zhang, M. Zhou, T. Zhao, X. Qin, X. Liu, M. Liu and P. Duan, *J. Phys. Chem. Lett.*, 2019, **10**, 3290–3295.
75 Q. Dai, H. Li, G. Sini and J. L. Bredas, *Adv. Funct. Mater.*, 2022, **32**, 2108662.
76 Y. H. Kim, R. Song, J. Hao, Y. Zhai, L. Yan, T. Moot, A. F. Palmstrom, R. Brunecky, W. You and J. J. Berry, *Adv. Funct. Mater.*, 2022, 2200454.

77 S. Jiang, Y. Song, H. Kang, B. Li, K. Yang, G. Xing, Y. Yu, S. Li, P. Zhao and T. Zhang, *ACS Appl. Mater. Interfaces*, 2021, **14**, 3385–3394.
78 C. Zhang, Z. S. Li, X. Y. Dong, Y. Y. Niu and S. Q. Zang, *Adv. Mater.*, 2022, **34**, 2109496.
79 J. Li, J. Li, R. Liu, Y. Tu, Y. Li, J. Cheng, T. He and X. Zhu, *Nat. Commun.*, 2020, **11**, 1–10.
80 T. Zhao, J. Han, P. Duan and M. Liu, *Acc. Chem. Res.*, 2020, **53**, 1279–1292.
81 D. Yang, P. Duan, L. Zhang and M. Liu, *Nat. Commun.*, 2017, **8**, 15727.
82 A. R. Lim, *Solid State Sci.*, 2019, **96**, 105955.
83 P. Tamarat, M. I. Bodnarchuk, J.-B. Trebbia, R. Erni, M. V. Kovalenko, J. Even and B. Lounis, *Nat. Mater.*, 2019, **18**, 717–724.
84 P. C. Sercel, J. L. Lyons, N. Bernstein and A. L. Efros, *J. Chem. Phys.*, 2019, **151**, 234106.
85 Y. Dai, Q. Wei, T. Chang, J. Zhao, S. Cao, B. Zou and R. Zeng, *J. Phys. Chem. C*, 2022, **126**, 11238–11245.
86 D. K. Russell, *J. Chem. Educ.*, 1996, **73**, 299.
87 Y. Zhang, C.-K. Lim, Z. Dai, G. Yu, J. W. Haus, H. Zhang and P. N. Prasad, *Phys. Rep.*, 2019, **795**, 1–51.
88 R. Kotlyar, T. Reinecke, M. Bayer and A. Forchel, *Phys. Rev. B: Condens. Matter Mater. Phys.*, 2001, **63**, 085310.
89 M. Fu, P. Tamarat, H. Huang, J. Even, A. L. Rogach and B. Lounis, *Nano Lett.*, 2017, **17**, 2895–2901.
90 M. Wang, Z. Yang and C. Zhang, *Adv. Opt. Mater.*, 2021, **9**, 2002236.
91 S. Hou, M. K. Gangishetty, Q. Quan and D. N. Congreve, *Joule*, 2018, **2**, 2421–2433.
92 A. Shapiro, M. W. Heindl, F. Horani, M.-H. Dahan, J. Tang, Y. Amouyal and E. Lifshitz, *J. Phys. Chem. C*, 2019, **123**, 24979–24987.
93 J. Yu, J. Kong, W. Hao, X. Guo, H. He, W. R. Leow, Z. Liu, P. Cai, G. Qian and S. Li, *Adv. Mater.*, 2019, **31**, 1806385.
94 Y. Shirahata and T. Oku, In Photovoltaic properties of Cu-doped $CH_3NH_3PbI_3$ with perovskite structure, *AIP Conf. Proc.*, 2017, **1807**(1), 020008.
95 B. Náfrádi, P. Szirmai, M. Spina, H. Lee, O. Yazyev, A. Arakcheeva, D. Chernyshov, M. Gibert, L. Forró and E. Horváth, *Nat. Commun.*, 2016, **7**, 1–8.
96 Y. Ping and J. Z. Zhang, *J. Phys. Chem. Lett.*, 2018, **9**, 6103–6111.
97 G. Zhan, J. Zhang, L. Zhang, Z. Ou, H. Yang, Y. Qian, X. Zhang, Z. Xing, L. Zhang and C. Li, *Nano Lett.*, 2022, **22**, 3961–3968.
98 T. Neumann, S. Feldmann, P. Moser, J. Zerhoch, T. van de Goor, A. Delhomme, T. Winkler, J. J. Finley, C. Faugeras and M. S. Brandt, 2020, DOI: **10.48550/arXiv.2009.13867**.
99 T. T. H. Do, A. S. Granados del Aguila, D. Zhang, J. Xing, S. Liu, M. Prosnikov, W. Gao, K. Chang, P. C. Christianen and Q. Xiong, *Nano Lett.*, 2020, **20**, 5141–5148.
100 K. Dulitz, A. Tauschinsky and T. P. Softley, *New J. Phys.*, 2015, **17**, 035005.
101 J.-Y. Chen, T.-M. Wong, C.-W. Chang, C.-Y. Dong and Y.-F. Chen, *Nat. Nanotechnol.*, 2014, **9**, 845–850.
102 O. L. Sanchez, D. Ovchinnikov, S. Misra, A. Allain and A. Kis, *Nano Lett.*, 2016, **16**, 5792–5797.
103 W. Ning, J. Bao, Y. Puttisong, F. Moro, L. Kobera, S. Shimono, L. Wang, F. Ji, M. Cuartero and S. Kawaguchi, *Sci. Adv.*, 2020, **6**, eabb5381.
104 K. M. Walsh, K. Pressler, M. J. Crane and D. R. Gamelin, *ACS Nano*, 2022, **16**, 2569–2576.
105 J. Lv, X. Yang and Z. Tang, *Adv. Mater.*, 2022, 2209539.
106 K. Yao, Y. Shen, Y. Li, X. Li, Y. Quan and Y. Cheng, *J. Phys. Chem. Lett.*, 2020, **12**, 598–603.
107 A. Monguzzi, J. Mezyk, F. Scotognella, R. Tubino and F. Meinardi, *Phys. Rev. B: Condens. Matter Mater. Phys.*, 2008, **78**, 195112.
108 M. Mitov, *Adv. Mater.*, 2012, **24**, 6260–6276.
109 R. Wang, S. Hu, X. Yang, X. Yan, H. Li and C. Sheng, *J. Mater. Chem. C*, 2018, **6**, 2989–2995.
110 A. Bokov and Z.-G. Ye, *J. Mater. Sci.*, 2006, **41**, 31–52.
111 A. V. Khaetskii, *Spin physics in semiconductors*, Springer, Berlin, 2008.
112 J. Wang, C. Zhang, H. Liu, R. McLaughlin, Y. Zhai, S. R. Vardeny, X. Liu, S. McGill, D. Semenov and H. Guo, *Nat. Commun.*, 2019, **10**, 129.
113 W. Li, Z. Wang, F. Deschler, S. Gao, R. H. Friend and A. K. Cheetham, *Nat. Rev. Mater.*, 2017, **2**, 1–18.
114 J. Yin, P. Maity, L. Xu, A. M. El-Zohry, H. Li, O. M. Bakr, J.-L. Brédas and O. F. Mohammed, *Chem. Mater.*, 2018, **30**, 8538–8545.
115 M. Wang, H. Zou, J. Zhang, T. Wu, H. Xu, S. Haacke and B. Hu, *J. Phys. Chem. Lett.*, 2020, **11**, 3647–3652.
116 W. Zhao, R. Su, Y. Huang, J. Wu, C. F. Fong, J. Feng and Q. Xiong, *Nat. Commun.*, 2020, **11**, 1–7.
117 M. T. Pham, E. Amerling, T. A. Ngo, H. M. Luong, K. Hansen, H. T. Pham, T. N. Vu, H. Tran, L. Whittaker-Brooks and T. D. Nguyen, *Adv. Opt. Mater.*, 2022, **10**, 2101232.
118 D. Powell, K. R. Hansen, L. Flannery and L. Whittaker-Brooks, *Acc. Chem. Res.*, 2021, **54**, 4371–4382.
119 K. Tanaka, T. Takahashi, T. Ban, T. Kondo, K. Uchida and N. Miura, *Solid State Commun.*, 2003, **127**, 619–623.
120 J. Even, L. Pedesseau and C. Katan, *J. Phy. Chem. C*, 2014, **118**, 11566–11572.
121 A. Manchon, H. C. Koo, J. Nitta, S. Frolov and R. Duine, *Nat. Mater.*, 2015, **14**, 871–882.
122 C. T. Wang, K. Chen, P. Xu, F. Yeung, H. S. Kwok and G. Li, *Adv. Funct. Mater.*, 2019, **29**, 1903155.
123 Z.-L. Gong, X. Zhu, Z. Zhou, S.-W. Zhang, D. Yang, B. Zhao, Y.-P. Zhang, J. Deng, Y. Cheng and Y.-X. Zheng, *Sci. China: Chem.*, 2021, **64**, 2060–2104.
124 A. Kondratov, M. Gorkunov, A. Darinskii, R. Gainutdinov, O. Rogov, A. Ezhov and V. Artemov, *Phys. Rev. B*, 2016, **93**, 195418.
125 C. Ye, J. Jiang, S. Zou, W. Mi and Y. Xiao, *J. Am. Chem. Soc.*, 2022, **144**, 9707–9714.
126 S. Jiang and N. A. Kotov, *Adv. Mater.*, 2022, 2108431.
127 M. Shiraishi and T. Ikoma, *Phys. E*, 2011, **43**, 1295–1317.
128 K. Ohtawara and H. Teramae, *Chem. Phys. Lett.*, 2004, **390**, 84–88.

129 J. Fischer, B. Trauzettel and D. Loss, *Phys. Rev. B: Condens. Matter Mater. Phys.*, 2009, **80**, 155401.
130 G. Long, Y. Zhou, M. Zhang, R. Sabatini, A. Rasmita, L. Huang, G. Lakhwani and W. Gao, *Adv. Mater.*, 2019, **31**, 1807628.
131 D. Han, C. Li, C. Jiang, X. Jin, X. Wang, R. Chen, J. Cheng and P. Duan, *Aggregate*, 2022, **3**, e148.
132 X. Ge, X. Qu, L. He, Y. Sun, X. Guan, Z. Pang, C. Wang, L. Yang, F. Wang and F. Rosei, *J. Mater. Chem. A*, 2019, **7**, 27225–27235.
133 J. Tian, G. Adamo, H. Liu, M. Klein, S. Han, H. Liu and C. Soci, *Adv. Mater.*, 2022, **34**, 2109157.
134 A. T. Young, *Appl. Opt.*, 1981, **20**, 533–535.
135 M. F. Maestre, C. Bustamante, T. L. Hayes, J. A. Subirana and I. Tinoco, *Nature*, 1982, **298**, 773–774.
136 L. Shi, L. Zhu, J. Guo, L. Zhang, Y. Shi, Y. Zhang, K. Hou, Y. Zheng, Y. Zhu and J. Lv, *Angew. Chem., Int. Ed.*, 2017, **56**, 15397–15401.
137 T. He, J. Li, X. Li, C. Ren, Y. Luo, F. Zhao, R. Chen, X. Lin and J. Zhang, *Appl. Phys. Lett.*, 2017, **111**, 151102.
138 M. Xu, X. Wu, Y. Yang, C. Ma, W. Li, H. Yu, Z. Chen, J. Li, K. Zhang and S. Liu, *ACS Nano*, 2020, **14**, 11130–11139.
139 W. Jiang, Z.-b Qu, P. Kumar, D. Vecchio, Y. Wang, Y. Ma, J. H. Bahng, K. Bernardino, W. R. Gomes and F. M. Colombari, *Science*, 2020, **368**, 642–648.

